

DIP: Differentiable Interreflection-aware Physics-based Inverse Rendering

Youming Deng
Wuhan University

Xueting Li
NVIDIA Research

Sifei Liu
NVIDIA Research

Ming-Hsuan Yang
UC Merced and Google

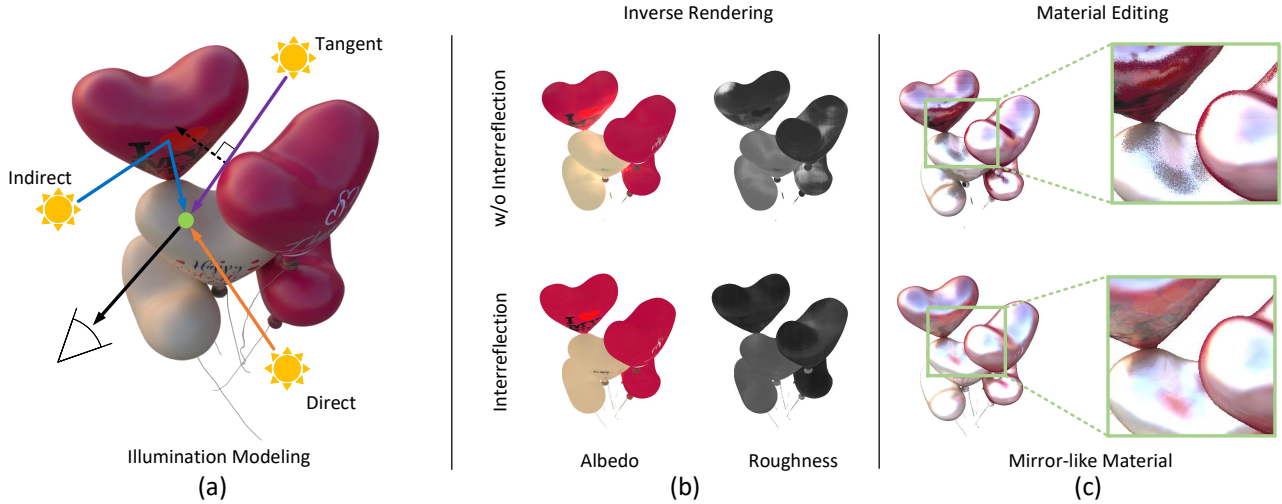


Figure 1. (a) Proposed interreflection-aware illumination model. (b) Inverse rendering results by our interreflection-aware illumination model and a baseline model [46] that does not model interreflection. (c) Material editing results. The effectiveness of explicit interreflection modeling can be best observed in (c), where our model successfully captures the reflection of the balloon as shown in the green box.

Abstract

We present a physics-based inverse rendering method that learns the illumination, geometry, and materials of a scene from posed multi-view RGB images. To model the illumination of a scene, existing inverse rendering works either completely ignore the indirect illumination or model it by coarse approximations, leading to sub-optimal illumination, geometry, and material prediction of the scene. In this work, we propose a physics-based illumination model that explicitly traces the incoming indirect lights at each surface point based on interreflection, followed by estimating each identified indirect light through an efficient neural network. Furthermore, we utilize the Leibniz’s integral rule to resolve non-differentiability in the proposed illumination model caused by one type of environment light – the tangent lights. As a result, the proposed interreflection-aware illumination model can be learned end-to-end together with geometry and materials estimation. As a side product, our physics-based inverse rendering model also facilitates flexible and realistic material editing as well as relighting. Extensive experiments on both synthetic and real-world

datasets demonstrate that the proposed method performs favorably against existing inverse rendering methods on novel view synthesis and inverse rendering. The source code and trained models will be released to the public at the project page: <https://denghilbert.github.io/dip/>.

1. Introduction

Inverse rendering aims to recover the illumination, geometry, and material simultaneously of a scene from multi-view images. Illumination plays an important role in inverse rendering by providing crucial lighting information for material and geometry estimation. However, it is challenging to accurately estimate illumination in a scene due to complex scene geometry and various materials that lead to light occlusion and interreflection. Early inverse rendering works [12, 20] adopt a simple illumination model [1] and can only be applied to scenes with simple geometry (e.g., scenes that only include a single object). Some recent approaches [17, 22, 39, 42, 43, 46] simulate natural illumination

by utilizing the rendering equation [14] for material editing and relighting. However, most of these methods [17, 42, 43] only model direct illumination and ignore indirect environment lights caused by occlusion and interreflection, leading to poor performance on cluttered scenes. Even when indirect lights are implicitly modeled as in [22, 39, 46], they are approximated with multi-layer perceptrons (MLPs), ignoring natural occlusion and interreflection knowledge in the scene. One example is shown in the top row of Fig. 1(b)(c) where the baseline model [46] fails to capture interreflection and produces noticeable artifacts in both inverse rendering and material editing.

To accurately model illumination as well as estimate the material and geometry of a cluttered scene, we propose a differentiable interreflection-aware physics-based inverse rendering framework, dubbed as *DIP*. For indirect illumination modeling, *DIP* first explicitly traces the incoming indirect lights at each surface point based on interreflection. It then estimates each traced indirect light through an efficient neural network. However, the interreflection-aware illumination model is not fully differentiable due to a special kind of environment lights – the tangent lights that fall rightly onto the brim of an object (purple ray in Fig. 1(a)). We first demonstrate how the tangent lights cause the non-differentiability and then develop a method to resolve this issue based on the Leibniz’s integral rule.

As a result, the proposed illumination module (green block of Fig. 2) can be learned end-to-end together with a novel refined sphere tracing module (blue block of Fig. 2), an SDF prediction MLP, and a material estimation auto-encoder (grey block of Fig. 2). During inference, *DIP* can be readily applied to novel view synthesis, material editing, and relighting, showing favorable performance compared to existing methods. The main contributions of this work are:

- We present an inverse rendering method for high-fidelity geometry, materials, and illumination estimation.
- We propose a novel interreflection-aware illumination module that explicitly models indirect illumination by tracing and estimating the incoming indirect lights at a surface point.
- We resolve the non-differentiability caused by the tangent lights in the proposed illumination model, enabling it to be learned end-to-end with a novel refined sphere tracing, geometry, and a material estimation module.
- The proposed method performs favorably against existing inverse rendering approaches on inverse rendering, novel-view synthesis, and material editing.

2. Related Work

Implicit Neural Networks. Implicit neural networks encode the geometry of a scene by predicting either occu-

pancy or a signed distance of each surface point. Early implicit neural networks [25, 28] are learned with ground truth occupancy or signed distances, while more recent models [26, 40] are trained with multi-view images by utilizing volume rendering [23]. However, by entangling geometry with appearance and illumination, these methods do not perform well on tasks such as material editing and free-viewpoint relighting. In this paper, we disentangle the geometry, material, and illumination by learning an inverse rendering framework, where the geometry is captured by an implicit neural network that predicts the signed distance value for each surface point.

Intrinsic Decomposition and Inverse Rendering. Intrinsic image decomposition [1] aims to model an image as the product of reflectance and shading. This is a highly ill-posed problem if ground truth annotation is not available. As a result, deep intrinsic decomposition models usually resort to synthetic dataset [2, 7, 9, 16, 27] or time-lapse sequences [19]. To better model image formulation and enable self-supervised decomposition from images, more recent methods further decompose shading into illumination and geometry, *i.e.*, inverse rendering. One line of self-supervised inverse rendering work [34, 37] utilizes the prior of a specific object category (*e.g.*, faces, cars, etc) to constrain illumination prediction. To apply inverse rendering on more general scenes, several methods use multi-view images as supervision [15, 41]. Recently, PhySG [43] and NeRFactor [45] merge implicit geometry with the rendering equation [14] to decompose material properties and illuminations from visual appearance. PhySG [43] resolves inverse rendering by modeling illumination as mixtures of spherical Gaussians [36], combined with an implicit function for geometry estimation. However, PhySG does not explicitly model indirect illumination, which plays an important role in capturing interreflection in a scene. To resolve this issue, several approaches [22, 32, 39, 45, 46] approximate the indirect illumination and visibility in the scene through MLPs. Nonetheless, without explicitly tracing and estimating indirect environment lights, these methods do not accurately capture the interreflection in the scene and produce artifacts in both inverse rendering and material editing. In contrast, we propose a self-supervised inverse rendering method that explicitly traces and estimates the indirect lights at each surface point, showing promising results in both inverse rendering and material editing.

3. Preliminaries

3.1. Rendering Equation

Before describing our method, we briefly review the Bidirectional Reflectance Distribution Function (BRDF) and the rendering equation that computes outgoing radiance at each surface point in the scene.

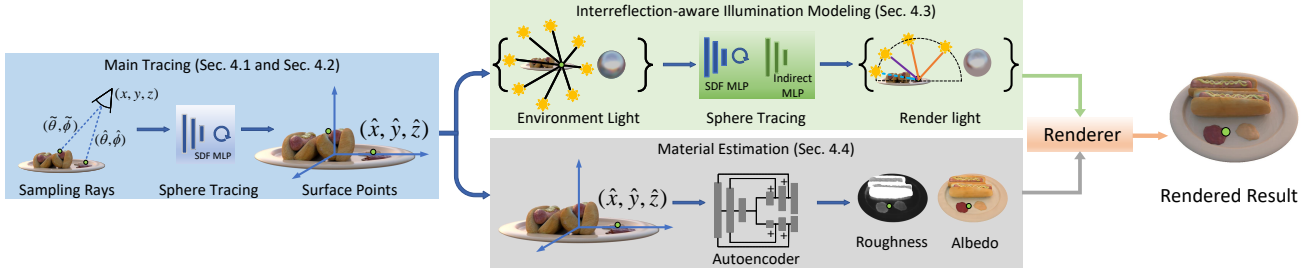


Figure 2. **Forward Rendering of DIP.** Given the camera parameters of a scene view, we sample a set of rays and trace the surface points hit by the rays by the sphere tracing with the refinement module introduced in Sec. 4.2. For each traced point, we estimate its illumination through the interreflection-aware illumination module in Sec. 4.3 and materials by the material estimation module in Sec. 4.4. Finally, we feed the estimated materials and illuminations to a differentiable renderer and render a target view image.

Given a surface point \mathbf{x} and the outgoing light direction ω_o , the rendering equation [14] computes the outgoing light $L_o(\omega_o; \mathbf{x})$ as the integral over all environment lights $L_i(\omega_i)$ from the upper hemisphere Ω :

$$L_o(\omega_o; \mathbf{x}) = \int_{\Omega} L_i(\omega_i) f_r(\omega_o, \omega_i; \mathbf{x}) (\omega_i \cdot \mathbf{n}) d\omega_i, \quad (1)$$

where $f_r(\omega_o, \omega_i; \mathbf{x})$ is the BRDF that models the reflectance property of the surface point \mathbf{x} and \mathbf{n} is the normal at this point. Based on the simplified Disney BRDF model [3], we further disentangle f_r as a constant albedo term $\frac{a}{\pi}$ accounting for diffuse while leaving the residue f_s representing the specularity at the surface point \mathbf{x} as:

$$f_r(\omega_o, \omega_i; \mathbf{x}) = \frac{a}{\pi} + f_s(\omega_o, \omega_i; \mathbf{x}). \quad (2)$$

We present the details of specularity modeling using the Microfacet model [5, 35] discussed in the supplementary.

3.2. Spherical Gaussians Function

We model the environment light $L_i(\omega_i)$, BRDF $f_r(\omega_o, \omega_i; \mathbf{x})$, and multiplication term $\omega_i \cdot \mathbf{n}$ in Eq. (17) by the Spherical Gaussian (SG) Distribution [36]. A Spherical Gaussian is defined as:

$$G(\omega_i; \boldsymbol{\xi}, \lambda, \boldsymbol{\mu}) = \boldsymbol{\mu} e^{\lambda(\omega_i \cdot \boldsymbol{\xi} - 1)}, \quad (3)$$

where $\omega_i \in \mathbb{S}^2$ is the input of the SG function, $\boldsymbol{\xi} \in \mathbb{S}^2$ is the lobe axis, $\lambda \in \mathbb{R}_+$ is the lobe sharpness, and $\boldsymbol{\mu} \in \mathbb{R}^3$ is the lobe amplitude.

When modeling the environment lights using the SG function, we assume the lights are uniformly cast from 128 infinitely faraway directions. We analyze the number of environment lights in Sec. 5.3. For computational efficiency, we further represent the BRDF f_r , and the multiplication term $\omega_i \cdot \mathbf{n}$ in Eq. (17) with SG as in [43]. More details can be found in the supplementary.

4. Proposed Method

Given multiple images of a scene, we learn a self-supervised inverse rendering framework that estimates the geometry, materials, and illumination of the scene. During inference, our model is readily available for novel view synthesis, relighting, and material editing. We show the overview of our pipeline in Fig. 2 and introduce details for geometry estimation (Sec. 4.1), surface point localization (Sec. 4.2), interreflection-aware illumination modeling (Sec. 4.3) and materials prediction (Sec. 4.4) below.

4.1. Geometry Estimation

We encode the geometry of a given scene by learning an MLP F_{SDF} that takes a query point $\mathbf{p} = (x, y, z)$ as input and predicts its SDF value (*i.e.*, the closest distance between \mathbf{p} and the object surface). We first pre-train this geometry MLP using multi-view images as in [39, 42, 46]. We then fine-tune the MLP together with the illumination and material estimation modules in the following sections.

4.2. Sphere Tracing with Refinement

We discuss how to locate all surface points by the learned geometry MLP discussed in Sec. 4.1 and a novel refined sphere tracing module.

Given camera parameters, classical sphere tracing algorithms [10, 21] trace all surface points by marching along sampled rays iteratively until reaching a point with an SDF value smaller than a given threshold τ . We demonstrate this tracing process in Fig. 3(a) and show the traced surface point \mathbf{p}_1 as well as the “true” surface point \mathbf{p}_2 in Fig. 3(b). As shown in Fig. 3, a larger threshold τ leads to a more inaccurate surface point location (*i.e.*, \mathbf{p}_1 is farther from the object surface), while a smaller threshold requires more tracing iterations. To efficiently and accurately locate a surface point, we propose a refinement process that directly steps from \mathbf{p}_1 to \mathbf{p}_2 . Our main observation is that as \mathbf{p}_1 moves closer to \mathbf{p}_2 , the surface curve sp_2 approximates to

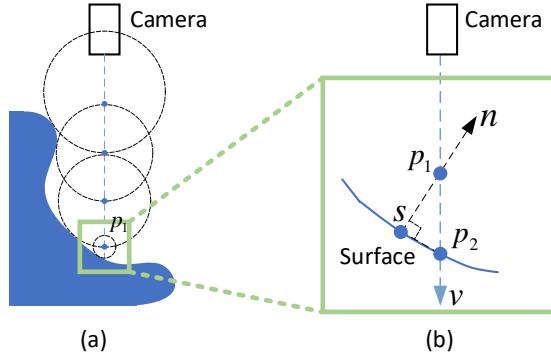


Figure 3. **Sphere Tracing with Refinement.** The classic sphere tracing algorithm stops at p_1 when the SDF value of this point is smaller than the threshold. We propose a refinement process that directly marches from p_1 to point p_2 that is closer to the surface.

a straight line. Thus we can find the length of $\overline{p_1 p_2}$ by:

$$\overline{p_1 p_2} = \frac{-F_{SDF}(p_1)}{v \cdot n}, \quad n = \frac{\nabla_p F_{SDF}(p)}{\|\nabla_p F_{SDF}(p)\|_2}, \quad (4)$$

where v is the normalized view direction, and the normal n at point s can be derived from the learned geometry MLP F_{SDF} discussed in Sec. 4.1.

Compared to classic sphere tracing methods [10, 21], the proposed refinement step not only reduces the tracing iteration number by allowing using a relatively larger threshold but also locates more accurate surface points.

4.3. Interreflection-aware Illumination

Illumination plays a critical role in recovering the geometry and materials of a scene from a set of RGB images. However, due to interreflection, it is challenging to accurately model the environment lights, especially indirect ones in a scene. Existing approaches either ignore the indirect lights [17, 42, 43] or implicitly approximate them [22, 39, 46] via neural networks.

In this work, we explicitly trace and estimate the incoming indirect lights at each surface point based on occlusion and reflectance. In addition, we analyze the *tangent lights* that cause non-differentiability in the illumination model. As our empirical experiments demonstrate in Tab. 1d, tangent lights are essential for accurate illumination estimation and cannot be simply ignored. Thus, we propose a differentiable method based on theoretical analysis to incorporate them into our illumination estimation module.

4.3.1 Environment Lights Classification via Tracing

For each environment light, we first classify it as a direct or indirect light by a simplified ray tracing process that explic-

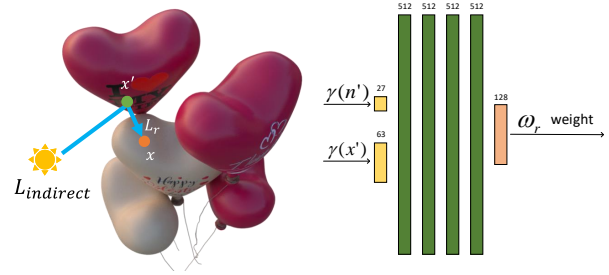


Figure 4. **Indirect MLP.** To estimate the indirect light at x coming from the reflected point x' , we feed the coordinates of x' with its normal n' into the indirect MLP F_{ind} and predict the weights used for environment lights aggregation. See Sec. 4.3 for details.

itly models interreflection.

Given a surface point x , we reversely trace each environment light starting from x to the light sources. Rays not obstructed by an object are classified as direct lights (orange rays in Fig. 1(a)), and obstructed rays are denoted as indirect lights (blue rays in Fig. 1(a)). We note that here we do not trace the full path of indirect light as classic ray tracing methods [18]. As long as a ray starting from the surface point hits an object while reaching the light sources, we classify the environment light as an indirect light and model it using the method discussed in Sec. 4.3.2. Although this efficient tracing process is simpler compared to methods that trace the complete path, we demonstrate its effectiveness with extensive experiments in Sec. 5.

4.3.2 Indirect Lights

As shown in Fig. 4, given each identified indirect light at the surface point x coming from a reflected point x' , we learn an MLP, F_{ind} , that explicitly formulates the indirect light by aggregating uniform environment lights. Specifically, for a target indirect light L_r , the MLP takes the coordinates and normal of the reflected point x' as inputs and predicts how much each environment light L^i contributes to L_r represented as a scalar weight $w_r^i \in \mathbb{R}$. Thus, the lobe sharpness λ_r and amplitude μ_r of L_r can be computed as:

$$\lambda_r = \sum_{i=1}^K w_r^i \cdot \lambda^i, \quad \mu_r = \sum_{i=1}^K w_r^i \cdot \mu^i, \quad (5)$$

$$w_r = F_{ind}(\gamma(x'), \gamma(n')), \quad (6)$$

where n' is the normal at x' with positional embedding γ [33], and K is the total environment light number (e.g., 128 in this work).

Compared to existing inverse rendering methods [22, 32, 39, 46], the proposed indirect light model has two advantages. First, interreflection in the scene is explicitly modeled through the explicit tracing and classification process

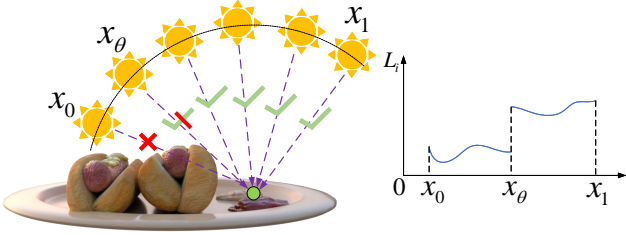


Figure 5. **Demonstration of Non-differentiability at Tangent Lights.** The tangent light x_θ changes abruptly from “obstructed” to “visible” at the boundary of the object, introducing a point of discontinuity and making Eq. (17) non-differentiable. This non-differentiability is also demonstrated by the figure on the right showing light intensity change w.r.t. the incoming light angle x_i .

discussed in Sec. 4.3.1. Second, instead of simply approximating the aggregation of indirect lights at a surface point by an MLP, we estimate each identified indirect light, leading to an illumination model with a higher capacity to better handle cluttered scenes. Fig. 6 and Fig. 7 empirically demonstrate the merits of our indirect light model.

4.3.3 Tangent Lights

Ideally, the identified direct lights in Sec. 4.3.1 and estimated indirect lights in Sec. 4.3.2 can be aggregated by Eq. (17) and learned by backpropagation. However, we note a class of environment light, “tangent lights” that fall right onto the brim of an object, making Eq. (17) non-differentiable. This is because tangent lights change abruptly at the object boundary from “obstructed” to “visible”, as shown in Fig. 5. A naive way to resolve this non-differentiable issue is to simply ignore tangent lights for the backpropagation process. However, such a naive solution does not consider errors from tangent lights and leads to inaccurate illumination estimation (see the last row of Tab. 1d). Instead, we propose to use the partial derivative with the Leibniz’s integral rule such that the gradient of the outgoing radiance w.r.t. all learnable parameters θ can be computed as:

$$\begin{aligned} \frac{\partial L_o(\omega_o; \mathbf{x})}{\partial \theta} &= \int_{\Omega'} \frac{\partial L_i(\omega_i) f_r(\omega_o, \omega_i; \mathbf{x})}{\partial \theta} (\omega_i \cdot \mathbf{n}) d\omega_i \\ &+ \int_{\partial\Omega} \left(\frac{\partial \omega_i}{\partial \theta} \cdot \mathbf{n}(\omega_i) \right) \Delta L_i(\omega_i) f_r(\omega_o, \omega_i; \mathbf{x}) (\omega_i \cdot \mathbf{n}) d\omega_i, \end{aligned} \quad (7)$$

where $\partial\Omega$ represents the edge (x_θ in Fig. 5) at which the light changes from “obstructed” to “visible”, $\Delta L_i(\omega_i) = L_i(\omega_i + \epsilon) - L_i(\omega_i - \epsilon)$ is the light difference of directions on $\partial\Omega$, and $\Omega' = \Omega - \partial\Omega$. We present the detailed mathematical deduction of Eq. (7) in the supplementary material.

To identify the tangent lights, we simply search for en-

vironment lights that are “almost” perpendicular (e.g., a 2-degree deviation) to the surface normal.

4.4. Material Estimation

For each surface point, we predict its roughness and albedo using a material autoencoder [11], as shown in the grey block of Fig. 2. Specifically, we first map the positional encoding [33] of the surface point coordinates into a latent vector through the material encoder. Then we decode the latent vector into roughness and albedo using two separate decoders. Given the estimated materials and illumination discussed in Sec. 4.3, we then render the scene from any given view direction with the rendering equation [14].

4.5. Training

We pre-train the geometry MLP F_{SDF} discussed in Sec. 4.1 following the MII [46]. This provides decent geometry information for the material and illumination module training. Next, we jointly train the geometry MLP, the material, and the illumination module by minimizing the L1 reconstruction loss ℓ_{rec} . We further encourage the material autoencoder to produce smooth roughness and albedo by applying a latent sparsity constraint ℓ_{KL} [6], and a smoothness loss ℓ_{smooth} [46]. The overall objective is:

$$\ell = \lambda_{rec} \ell_{rec} + \lambda_{KL} \ell_{KL} + \lambda_{smooth} \ell_{smooth}, \quad (8)$$

$$\ell_{KL} = \sum_{i=1}^N KL(\rho || z_i), \quad (9)$$

$$\ell_{smooth} = ||D(\mathbf{z}) - D(\mathbf{z} + \epsilon)||, \quad (10)$$

where N is the dimension of latent vector \mathbf{z} , and D represents the decoders in the material autoencoder. We set ρ to be 0.05 and ϵ to be 0.02. The weights are set to be $\lambda_{rec} = 1.0$, $\lambda_{KL} = 0.01$, $\lambda_{smooth} = 0.1$.

To summarize, given multi-view images of a scene, our framework models its: (1) *illumination* via a set of learnable environment lights represented as SGs $\{\xi_i, \lambda_i, \mu_i\}_{i=1}^{128}$, (2) *geometry* via an MLP F_{SDF} , (3) *material* property (i.e., albedo \mathbf{a} and roughness R for each surface point) via a material autoencoder.

5. Experimental Results

5.1. Synthetic Dataset

We evaluate our method on the synthetic scenes in [46]. All the scenes are rendered with natural environment lights and provided with foreground masks. For quantitative evaluation, the dataset provides 200 testing images along with the ground truth albedo and roughness. The images have a resolution of 800×800 .

#Train/Test (HxW)	Synthetic Chair 200/200 (800x800)			Synthetic Jugs 100/200 (800x800)			Synthetic Air Balloons 100/200 (800x800)			Synthetic Hotdog 100/200 (800x800)		
	Metrics	↓LPIPS	↑SSIM	↑PSNR	↓LPIPS	↑SSIM	↑PSNR	↓LPIPS	↑SSIM	↑PSNR	↓LPIPS	↑SSIM
PhySG* [43]	0.0406	0.9497	32.08	0.0515	0.9742	33.59	0.0439	0.9618	31.79	0.0317	0.9564	31.95
MII [46]	0.0147	0.9482	35.42	0.0193	0.9714	37.47	0.0468	0.9498	31.03	0.0216	0.9531	32.69
Ours	0.0125	0.9534	36.04	0.0148	0.9788	38.76	0.0364	0.9613	32.72	0.0192	0.9589	33.76

(a) Novel View Synthesis.

#Train/Test (HxW)	Synthetic Chair 200/200 (800x800)			Synthetic Jugs 100/200 (800x800)			Synthetic Air Balloons 100/200 (800x800)			Synthetic Hotdog 100/200 (800x800)		
	Metrics	↓LPIPS	↑SSIM	↑PSNR	↓LPIPS	↑SSIM	↑PSNR	↓LPIPS	↑SSIM	↑PSNR	↓LPIPS	↑SSIM
PhySG* [43]	0.1004	0.9159	24.58	0.2119	0.9415	27.38	0.1395	0.9405	24.51	0.1517	0.9229	19.51
MII [46]	0.1158	0.9063	24.96	0.2302	0.9216	26.719	0.1636	0.9218	22.53	0.0770	0.9401	23.64
Ours	0.0881	0.9083	25.07	0.2138	0.9477	26.80	0.1147	0.9513	26.43	0.0887	0.9415	22.77

(b) Albedo Estimation.

scenes	Synthetic Chair		Synthetic Jugs		Synthetic Air Balloons		Synthetic Hotdog	
	↓MSE	↓ARE	↓MSE	↓ARE	↓MSE	↓ARE	↓MSE	↓ARE
PhySG* [43]	0.0921	1.1771	0.1200	1.2974	0.1832	3.0347	0.2861	24.6206
MII [46]	0.0306	1.1861	0.0617	1.1789	0.0242	0.8936	0.0776	4.7174
Ours	0.0421	1.0829	0.0484	0.9123	0.0132	0.6450	0.0819	4.5096

(c) Roughness Estimation.

Scenes	Chair	Jugs	Air Balloons	Hotdog
	Metric			
↓Light Estimation MSE				
PhySG* [43]	0.0557	0.1067	0.0154	0.0493
MII [46]	0.0562	0.1371	0.0186	0.0256
Ours	0.0232	0.0555	0.0120	0.0144
Ours (w/o tangent)	0.0386	0.0699	0.0213	0.0427

(d) Light Estimation.

Table 1. **Quantitative Results.** We compare our method with PhySG* [43] (slightly modified, see Sec. 5.2) and MII [46] on four tasks: novel view synthesis, albedo, and roughness estimation, as well as environment map estimation. HDR images used in synthetic data are tone mapped with $I_{new} = I_{old}^{1/2.2}$ and clipped to $[0, 1]$.

5.2. Comparisons with State-of-the-art Methods

Baseline methods. We compare with two state-of-the-art inverse rendering methods: PhySG [43] and MII [46]. Both methods predict illumination, materials, and geometry from multi-view images. Following MII [46], we replace the global roughness module in PhySG [43] with our spatial-varying material net since the original one cannot estimate surface roughness.

Metrics. We conduct extensive experiments to compare the proposed method and baselines on novel view synthesis, materials estimation, and environment lights prediction. Specifically, for novel view synthesis and albedo prediction, we report the PSNR, SSIM, and LPIPS [44] between the ground truth and predictions. For roughness estimation, we adopt the mean square error (MSE) and the absolute relative error [30] as evaluation metrics. While for illumination estimation, we compare the MSE between the ground truth and predicted environment maps as in [4].

Quantitative Results. We report quantitative evaluation on novel view synthesis, materials, and illumination evaluation in Tab. 1. We use ground truth images, albedo, roughness, and environment maps to compute the metrics discussed above. As shown in Tab. 1a and Tab. 1d, our method consistently outperforms the baseline models on all testing scenes on novel view synthesis and illumination estimation. For material estimation, our method performs favorably against baselines on all testing scenes and most metrics quantita-

tively, as demonstrated in Tab. 1b and Tab. 1c.

Qualitative Comparisons of Indirect Light. We show qualitative results in Fig. 6. Without modeling indirect illumination, PhySG [43] does not predict correct roughness and cannot disentangle the illumination with materials where the lights are obstructed (*e.g.*, the occluded jug bottoms and the white balloon in the middle). In contrast, our method predicts more consistent roughness and realistic albedo by explicitly tracing and estimating indirect lights based on occlusion and reflectance.

Qualitative Comparisons of Interreflection. We show that our model effectively captures the interreflection in a scene by changing the Fresnel coefficient [3] in the Fresnel term¹. To this end, we increase the coefficient to make the objects more mirror-like, as shown in Fig. 7(b). Surprisingly, our model can capture the interreflection in every scene. We observe the reflected heart-shaped pattern in the balloon scene in Fig. 1(c), the shadows of the back of the chair and pillow accurately casting onto the seat, and the precise edge shape of the hotdog projecting on the plate (green boxes in Fig. 7(b)). In contrast, the same editing applied to the MII [46] generates noticeable artifacts for interreflection. This empirically demonstrates that the proposed method successfully mimics the reflectance in the physical world, which is rarely achieved by existing mod-

¹Fresnel term models how much light leaves the object surface with a given arbitrary direction of incidence.

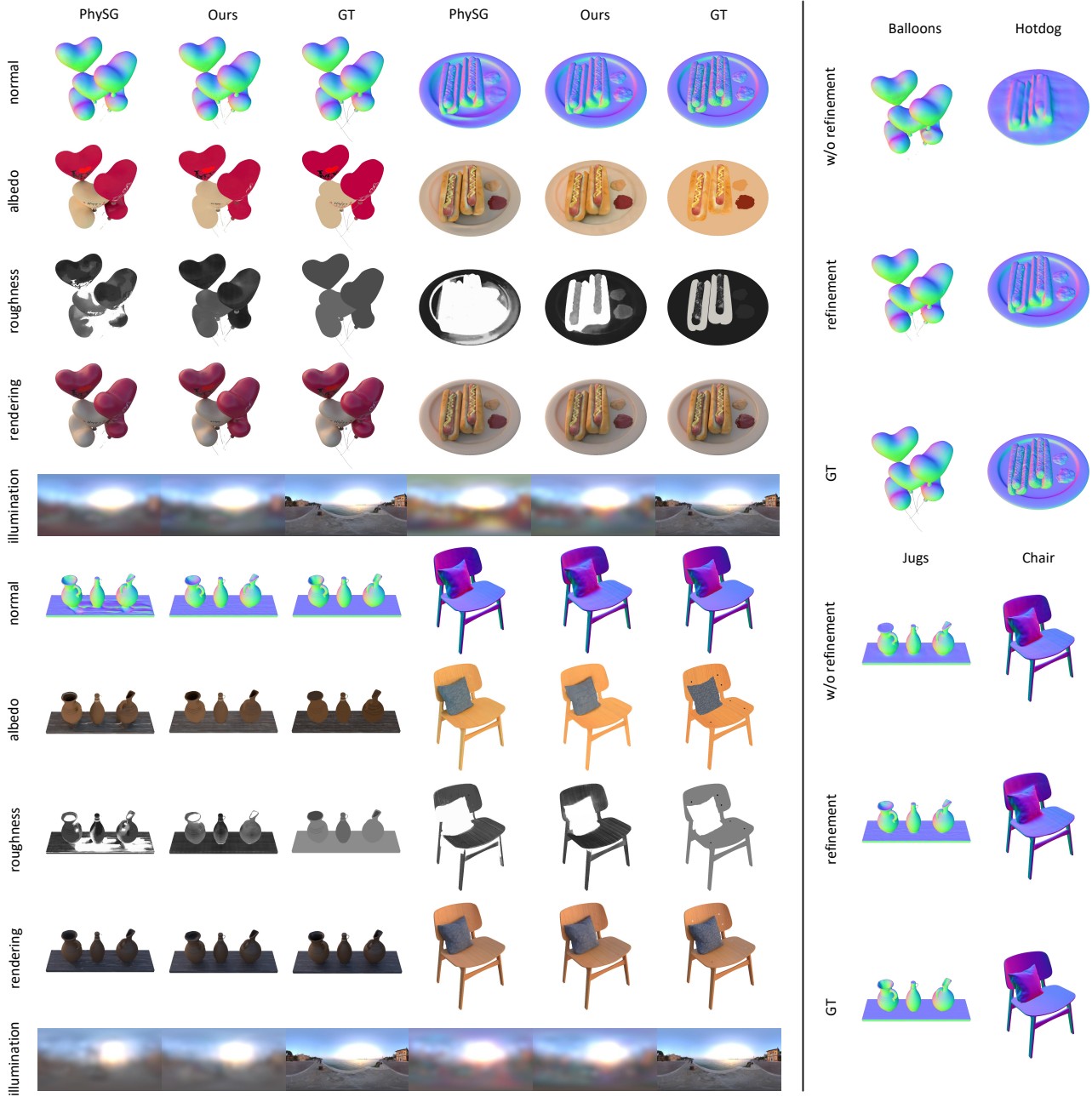


Figure 6. **Qualitative Comparisons.** *Left:* We show qualitative comparisons of PhySG [43] and our method on novel view synthesis, albedo, roughness, and environment map estimation. *Right:* We demonstrate the contribution of the proposed refinement for sphere tracing by comparing object surface normal.

els [22, 39, 46].

Qualitative Results for Relighting and Material Editing.

Thanks to the rendering equation, our model facilitates flexible editing for both material and illumination during inference. We demonstrate how to edit the learned albedo in Fig. 7(a, I), the roughness in the right of Fig. 7(a) and the environment light in Fig. 7(a, III)(a, IV). Our framework

can get reasonable rendering results with different base colors or environment illumination. More results and videos are available in the supplementary material.

5.3. Ablation Studies

Sphere Tracing Refinement. To demonstrate the effectiveness of the refinement process discussed in Sec. 4.2, we

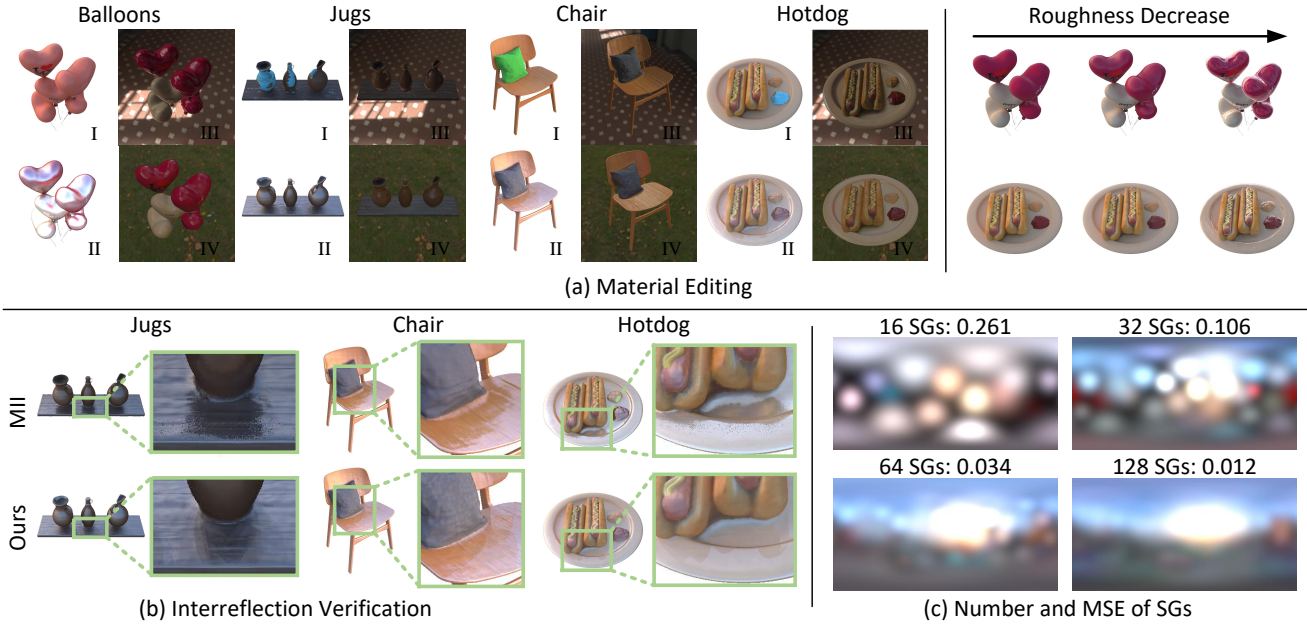


Figure 7. **Material Editing and Relighting.** (a) *Left:* Material editing and relighting results by changing the albedo and illumination. *Right:* By gradually decreasing the surface roughness, the object’s surface successfully changes from a matte surface to a smooth one. (b) Interreflection modeling comparison between our model and [46] by changing the material of the objects to be mirror-like. (c) We experiment with different SG numbers for illumination to find a balance between a high-fidelity model and memory efficiency.

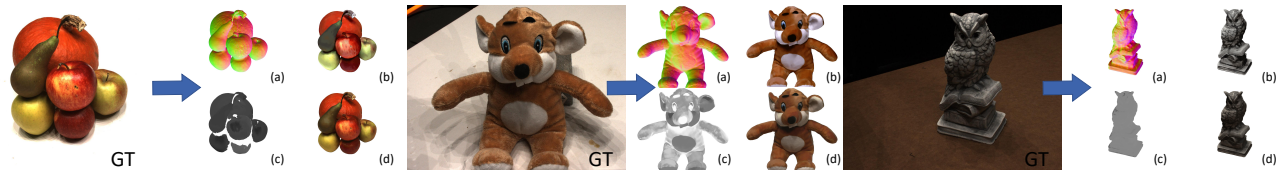


Figure 8. **Qualitative Results on DTU [13].** Even for the real-world dataset, DIP can still decompose reasonable (a) normal, (b) albedo, (c) roughness, and (d) rendering results. The generality of DIP is verified on DTU MVS dataset [13].

perform ablation studies by removing this refinement process. The results are shown in Fig. 6 (right). Without this refinement process, the model cannot capture the geometry details in the hot dog scene, the ribbons below the balloons, and the surface of the balloons presents noticeable artifacts. **Tangent Lights.** To avoid the non-differentiable issue, a naive solution is to remove all the tangent light for the rendering. However, the last row of Tab. 1d shows that the light estimation without tangent lights is unsatisfying compared to our full model. As shown in Tab. 1d, tangent lights are crucial to estimate realistic environment lights. Without modeling tangent lights, the predicted environment lights are noisy and inconsistent. More comparisons can be found in the supplementary material.

Spherical Gaussian Number. The number of environment lights determines how smoothly the lights are modeled. In Fig. 7(c), the quality of light estimation improves when Spherical Gaussians are used. In this work, we use 128 en-

vironment lights as a trade-off between quality and memory efficiency.

5.4. Evaluation on Real-World Images

We demonstrate the generalization ability of the proposed method by applying it to the DTU MVS dataset [13]. We select objects with diverse materials for these experiments, including a furry bear, a rough owl, and highly occluded fruits. We estimate the camera pose by using the COLMAP method [31]. Photos in the DTU dataset are taken in a black room with LED above the scenes. As a result, the environment illumination is not from an infinitely far distance as assumed in Appendix A and is challenging for inverse rendering. When using two separate decoders for albedo and roughness estimation, the model is prone to trivial solutions – all roughness saturates to the max roughness value instead of being spatially varying. The trivial solution can be resolved by sharing more layers between

the albedo and roughness decoders. Intuitively, this design adds a mutual constraint on roughness and albedo estimation as a regularization to avoid trivial solutions. With this design, our method can decompose each scene into reasonable albedo, roughness, and geometry normal in Fig. 8. More results and analysis on the DTU MVS dataset can be found in the supplementary.

6. Conclusion

In this paper, we introduce DIP – an inverse rendering framework that simultaneously predicts the illumination, geometry, and material of a scene from multi-view images. Through explicitly tracing and estimating indirect lights at each surface point, DIP effectively captures the interreflection in the scene. We demonstrate the effectiveness of DIP for inverse rendering, material editing, and free-viewpoint relighting on both real and synthetic datasets, achieving favorable performance against state-of-the-art inverse rendering models.

References

- [1] Harry Barrow, J Tenenbaum, A Hanson, and E Riseman. Recovering intrinsic scene characteristics. Technical Report 157, SRI International, 1978. 1, 2
- [2] Sai Bi, Nima Khademi Kalantari, and Ravi Ramamoorthi. Deep hybrid real and synthetic training for intrinsic decomposition. *EGSR*, 2018. 2
- [3] Brent Burley and Walt Disney Animation Studios. Physically-based shading at Disney. In *SIGGRAPH*, 2012. 3, 6, 11, 13
- [4] Blender Online Community. Blender - a 3d modelling and rendering package. 2020. 6
- [5] Robert L. Cook and Kenneth E. Torrance. A reflectance model for computer graphics. *TOG*, 1982. 3, 11
- [6] Ingrid Daubechies, Michel Defrise, and Christine De Mol. An iterative thresholding algorithm for linear inverse problems with a sparsity constraint. *Communications on Pure and Applied Mathematics*, 2004. 5
- [7] Qingnan Fan, Jiaolong Yang, Gang Hua, Baoquan Chen, and David Wipf. Revisiting deep intrinsic image decompositions. 2018. 2
- [8] Harley Flanders. Differentiation under the integral sign. *The American Mathematical Monthly*, 1973. 12
- [9] Guangyun Han, Xiaohua Xie, Jianhuang Lai, and Wei-Shi Zheng. Learning an intrinsic image decomposer using synthesized rgb-d dataset. *IEEE Signal Processing Letters*, 2018. 2
- [10] John C. Hart. Sphere tracing: a geometric method for the antialiased ray tracing of implicit surfaces. *Visual Computer*, 1996. 3, 4
- [11] Geoffrey E Hinton and Ruslan R Salakhutdinov. Reducing the dimensionality of data with neural networks. *Science*, 2006. 5
- [12] Michael Janner, Jiajun Wu, Tejas D. Kulkarni, Ilker Yildirim, and Josh Tenenbaum. Self-supervised intrinsic image decomposition. In *NeurIPS*, 2017. 1
- [13] Rasmus Jensen, Anders Dahl, George Vogiatzis, Engil Tola, and Henrik Aanæs. Large scale multi-view stereopsis evaluation. In *CVPR*, 2014. 8, 14
- [14] James T. Kajiya. The rendering equation. In *SIGGRAPH*, 1986. 2, 3, 5, 11
- [15] Kichang Kim, Akihiko Torii, and Masatoshi Okutomi. Multi-view inverse rendering under arbitrary illumination and albedo. In *ECCV*, 2016. 2
- [16] Louis Lettry, Kenneth Vanhoey, and Luc Van Gool. Darn: a deep adversarial residual network for intrinsic image decomposition. In *WACV*, 2018. 2
- [17] Junxuan Li and Hongdong Li. Self-calibrating photometric stereo by neural inverse rendering. In *ECCV*, 2022. 1, 2, 4
- [18] Tzu-Mao Li, Miika Aittala, Frédo Durand, and Jaakko Lehtinen. Differentiable monte carlo ray tracing through edge sampling. *TOG*, 2018. 4
- [19] Zhengqi Li and Noah Snavely. Cgintrinsics: Better intrinsic image decomposition through physically-based rendering. In *ECCV*, 2018. 2
- [20] Zhengqin Li, Zexiang Xu, Ravi Ramamoorthi, Kalyan Sunkavalli, and Manmohan Chandraker. Learning to reconstruct shape and spatially-varying reflectance from a single image. *TOG*, 2018. 1, 12
- [21] Shaohui Liu, Yinda Zhang, Songyou Peng, Boxin Shi, Marc Pollefeys, and Zhaopeng Cui. DIST: rendering deep implicit signed distance function with differentiable sphere tracing. In *CVPR*, 2020. 3, 4
- [22] Linjie Lyu, Marc Habermann, Lingjie Liu, Mallikarjun B. R., Ayush Tewari, and Christian Theobalt. Efficient and differentiable shadow computation for inverse problems. In *ICCV*, 2021. 1, 2, 4, 7
- [23] Nelson L. Max. Optical models for direct volume rendering. *TVCG*, 1995. 2
- [24] Julian Meder and Beat D. Bröderlin. Hemispherical gaussians for accurate light integration. In *ICCVG*, 2018. 11
- [25] Lars M. Mescheder, Michael Oechsle, Michael Niemeyer, Sebastian Nowozin, and Andreas Geiger. Occupancy networks: Learning 3d reconstruction in function space. In *CVPR*, 2019. 2
- [26] Ben Mildenhall, Pratul P. Srinivasan, Matthew Tancik, Jonathan T. Barron, Ravi Ramamoorthi, and Ren Ng. Nerf: Representing scenes as neural radiance fields for view synthesis. In *ECCV*, 2020. 2
- [27] Takuya Narihira, Michael Maire, and Stella X. Yu. Direct intrinsics: Learning albedo-shading decomposition by convolutional regression. In *ICCV*, 2015. 2
- [28] Jeong Joon Park, Peter Florence, Julian Straub, Richard A. Newcombe, and Steven Lovegrove. DeepSDF: Learning continuous signed distance functions for shape representation. In *CVPR*, 2019. 2
- [29] Osborne Reynolds. *Papers on mechanical and physical subjects: the sub-mechanics of the universe*. University Press, 1903. 11, 12

- [30] Ashutosh Saxena, Min Sun, and Andrew Y. Ng. Make3d: Learning 3d scene structure from a single still image. *TPAMI*, 2009. [6](#)
- [31] Johannes Lutz Schönberger and Jan-Michael Frahm. Structure-from-motion revisited. In *CVPR*, 2016. [8](#)
- [32] Pratul P. Srinivasan, Boyang Deng, Xiuming Zhang, Matthew Tancik, Ben Mildenhall, and Jonathan T. Barron. Nerv: Neural reflectance and visibility fields for relighting and view synthesis. In *CVPR*, 2021. [2](#), [4](#)
- [33] Matthew Tancik, Pratul Srinivasan, Ben Mildenhall, Sara Fridovich-Keil, Nithin Raghavan, Utkarsh Singhal, Ravi Ramamoorthi, Jonathan Barron, and Ren Ng. Fourier features let networks learn high frequency functions in low dimensional domains. In *NeurIPS*, 2020. [4](#), [5](#)
- [34] Ayush Tewari, Michael Zollhofer, Hyeonwoo Kim, Pablo Garrido, Florian Bernard, Patrick Perez, and Christian Theobalt. Mofa: Model-based deep convolutional face autoencoder for unsupervised monocular reconstruction. In *ICCV*, 2017. [2](#)
- [35] Bruce Walter, Stephen R. Marschner, Hongsong Li, and Kenneth E. Torrance. Microfacet models for refraction through rough surfaces. In *EGSR*, 2007. [3](#), [11](#)
- [36] Jiaping Wang, Peiran Ren, Minmin Gong, John M. Snyder, and Baining Guo. All-frequency rendering of dynamic, spatially-varying reflectance. *TOG*, 2009. [2](#), [3](#)
- [37] Shangzhe Wu, Christian Rupprecht, and Andrea Vedaldi. Unsupervised learning of probably symmetric deformable 3d objects from images in the wild. In *CVPR*, 2020. [2](#)
- [38] Kun Xu, Yan-Pei Cao, Li-Qian Ma, Zhao Dong, Rui Wang, and Shi-Min Hu. A practical algorithm for rendering all-frequency interreflections. *ACM TOG*, 2014. [11](#)
- [39] Wenqi Yang, Guanying Chen, Chaofeng Chen, Zhenfang Chen, and Kwan-Yee K. Wong. Ps-nerf: Neural inverse rendering for multi-view photometric stereo. In *ECCV*, 2022. [1](#), [2](#), [3](#), [4](#), [7](#)
- [40] Lior Yariv, Yoni Kasten, Dror Moran, Meirav Galun, Matan Atzmon, Ronen Basri, and Yaron Lipman. Multiview neural surface reconstruction by disentangling geometry and appearance. In *NeurIPS*, 2020. [2](#)
- [41] Ye Yu and William A. P. Smith. Inverserendernet: Learning single image inverse rendering. In *CVPR*, 2019. [2](#)
- [42] Kai Zhang, Fujun Luan, Zhengqi Li, and Noah Snavely. IRON: inverse rendering by optimizing neural sdfs and materials from photometric images. In *CVPR*, 2022. [1](#), [2](#), [3](#), [4](#)
- [43] Kai Zhang, Fujun Luan, Qianqian Wang, Kavita Bala, and Noah Snavely. Physg: Inverse rendering with spherical gaussians for physics-based material editing and relighting. In *CVPR*, 2021. [1](#), [2](#), [3](#), [4](#), [6](#), [7](#), [13](#), [15](#), [16](#), [17](#), [18](#)
- [44] Richard Zhang, Phillip Isola, Alexei A. Efros, Eli Shechtman, and Oliver Wang. The unreasonable effectiveness of deep features as a perceptual metric. In *CVPR*, 2018. [6](#)
- [45] Xiuming Zhang, Pratul P. Srinivasan, Boyang Deng, Paul E. Debevec, William T. Freeman, and Jonathan T. Barron. Ner-factor: neural factorization of shape and reflectance under an unknown illumination. *TOG*, 2021. [2](#)
- [46] Yuanqing Zhang, Jiaming Sun, Xingyi He, Huan Fu, Rongfei Jia, and Xiaowei Zhou. Modeling indirect illumination for inverse rendering. In *CVPR*, 2022. [1](#), [2](#), [3](#), [4](#), [5](#), [6](#), [7](#), [8](#), [13](#), [15](#), [16](#), [17](#), [18](#)

Supplementary Material for DIP: Differentiable Interreflection-aware Physics-based Inverse Rendering

In this supplementary material, we first introduce the Spherical Gaussians (SGs) function, the multiplications of SGs in Appendix A, and how to use SGs to represent terms in the rendering equation in Appendix B. Then we prove how to solve the non-differentiability at tangent lights on one dimension and use the Reynolds transport theorem [29] to extend to a higher dimension in Appendix C. After that, the detail of network architecture is introduced in Appendix D. Moreover, we compare two material decoder designs in Appendix E and show comprehensive qualitative results in Appendix F. Finally, we discuss the limitations of our method in Appendix G.

A. Spherical Gaussians Function

A.1. Representation of SGs

A general form of SGs can be represented as:

$$G(\mathbf{x}; \boldsymbol{\xi}, \lambda, \boldsymbol{\mu}) = \boldsymbol{\mu} e^{\lambda(\mathbf{x} \cdot \boldsymbol{\xi} - 1)}, \quad (11)$$

where $\mathbf{x} \in \mathbb{S}^2$ is the input of SGs function, $\boldsymbol{\xi} \in \mathbb{S}^2$ is the lobe axis, $\lambda \in \mathbb{R}_+$ is the lobe sharpness, and $\boldsymbol{\mu} \in \mathbb{R}^3$ is the lobe amplitude.

A.2. Multiplication of SGs

Following [38], we represent the multiplication of two different SGs $G(\mathbf{x}; \boldsymbol{\xi}_1, \lambda_1, \boldsymbol{\mu}_1)$ and $G(\mathbf{x}; \boldsymbol{\xi}_2, \lambda_2, \boldsymbol{\mu}_2)$ using a third one $G(\mathbf{x}; \boldsymbol{\xi}', \lambda', \boldsymbol{\mu}')$:

$$\begin{aligned} G_1 \cdot G_2 &= \boldsymbol{\mu}_1 e^{\lambda_1(\mathbf{x} \cdot \boldsymbol{\xi}_1 - 1)} \cdot \boldsymbol{\mu}_2 e^{\lambda_2(\mathbf{x} \cdot \boldsymbol{\xi}_2 - 1)} \\ &= \boldsymbol{\mu}' e^{\lambda'(\mathbf{x} \cdot \boldsymbol{\xi}' - 1)}, \end{aligned} \quad (12)$$

where

$$\boldsymbol{\mu}' = \boldsymbol{\mu}_1 \boldsymbol{\mu}_2 e^{\lambda_3 - \lambda_1 - \lambda_2}, \quad (13)$$

$$\lambda' = \lambda_3 = \|\lambda_1 \boldsymbol{\xi}_1 + \lambda_2 \boldsymbol{\xi}_2\|, \quad (14)$$

$$\|\lambda_1 \boldsymbol{\xi}_1 + \lambda_2 \boldsymbol{\xi}_2\| = \sqrt{\lambda_1^2 + \lambda_2^2 + 2\lambda_1 \lambda_2 (\boldsymbol{\xi}_1 \cdot \boldsymbol{\xi}_2)}, \quad (15)$$

$$\boldsymbol{\xi}' = \frac{\lambda_1 \boldsymbol{\xi}_1 + \lambda_2 \boldsymbol{\xi}_2}{\lambda_3}. \quad (16)$$

B. Rendering Equation Representation

The rendering equation [14] used in the submission is:

$$L_o(\boldsymbol{\omega}_o; \mathbf{x}) = \int_{\Omega} L_i(\boldsymbol{\omega}_i) f_r(\boldsymbol{\omega}_o, \boldsymbol{\omega}_i; \mathbf{x}) (\boldsymbol{\omega}_i \cdot \mathbf{n}) d\boldsymbol{\omega}_i. \quad (17)$$

where $L_i(\boldsymbol{\omega}_i)$ is the incident light, $f_r(\boldsymbol{\omega}_o, \boldsymbol{\omega}_i; \mathbf{x})$ is simplified Disney BRDF model [3] at the surface point \mathbf{x} and \mathbf{n} is the normal at this point.

We discuss how to represent each part in the rendering equation using SGs. It is worth noticing that we only consider a *single incidence direction* $\boldsymbol{\omega}_i$ in the following part for simplicity.

B.1. Incident (Environment) Light

We simulate continuous environment illumination as composed of different discrete light sources:

$$L_i(\boldsymbol{\omega}_i) = \boldsymbol{\mu} e^{\lambda(\boldsymbol{\omega}_i \cdot \boldsymbol{\xi} - 1)}, \quad (18)$$

where $\boldsymbol{\omega}_i \in \mathbb{S}^2$ is the input of incident light SGs function, $\boldsymbol{\xi} \in \mathbb{S}^2$ is the lobe axis, $\lambda \in \mathbb{R}_+$ is the lobe sharpness, and $\boldsymbol{\mu} \in \mathbb{R}^3$ is the lobe amplitude.

B.2. Representing $\boldsymbol{\omega}_i \cdot \mathbf{n}$ as SGs

The multiplication of the view direction $\boldsymbol{\omega}_i$ and surface normal \mathbf{n} can also be transformed into SGs [24] as:

$$\begin{aligned} \boldsymbol{\omega}_i \cdot \mathbf{n} &= G(\boldsymbol{\omega}_i; 0.0315, \mathbf{n}, 32.7080) - 31.7003 \\ &= 32.7080 \cdot e^{\mathbf{n}(\boldsymbol{\omega}_i \cdot 0.0315 - 1)} - 31.7003. \end{aligned} \quad (19)$$

B.3. Specular Term in BRDF

The simplified Disney BRDF model [3] split reflectance into diffuse and specular:

$$f_r(\boldsymbol{\omega}_o, \boldsymbol{\omega}_i; \mathbf{x}) = \frac{a}{\pi} + f_s(\boldsymbol{\omega}_o, \boldsymbol{\omega}_i; \mathbf{x}) \quad (20)$$

We have explained the first term in the submission, and the second term f_s is modeled with the Microfacet Model [5, 35]:

$$f_s(\boldsymbol{\omega}_o, \boldsymbol{\omega}_i; \mathbf{x}) = \frac{F(\boldsymbol{\omega}_o, \boldsymbol{\omega}_i) \mathbf{G}(\boldsymbol{\omega}_o, \boldsymbol{\omega}_i) D(\mathbf{h})}{4 \cdot (\mathbf{n} \cdot \boldsymbol{\omega}_o)(\mathbf{n} \cdot \boldsymbol{\omega}_i)}, \quad (21)$$

There are three important terms (F , \mathbf{G} , D) to simulate specular:

- Fresnel term F that evaluates how much light is reflected by the surface under a given angle of incidence.
- Geometric attenuation term \mathbf{G} (*i.e.*, masking and shadowing term) that accounts for mutual shadowing and masking of microfacets.
- A microfacet distribution function D that tells what fraction of microfacets are oriented in direction $\mathbf{h} = \frac{\boldsymbol{\omega}_o + \boldsymbol{\omega}_i}{\|\boldsymbol{\omega}_o + \boldsymbol{\omega}_i\|_2}$ so that light incoming from direction $\boldsymbol{\omega}_i$ will be reflected in direction $\boldsymbol{\omega}_o$.

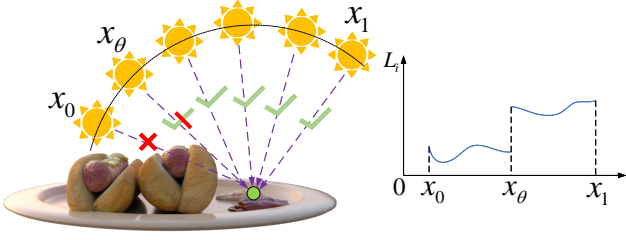


Figure 9. **Demonstration of Non-differentiability at Tangent Lights.** We borrow the figure in the main body here for the explanation.

We represent each term as in [20]:

$$F(\omega_o, \omega_i) = S + (1 - S) \cdot 2^{-(5.55473\omega_o \cdot \mathbf{h} + 6.8316)(\omega_o \cdot \mathbf{h})}, \quad (22)$$

$$\mathbf{G}(\omega_o, \omega_i) = \frac{\omega_o \cdot \mathbf{n}}{\omega_o \cdot \mathbf{n}(1 - k) + k} \cdot \frac{\omega_i \cdot \mathbf{n}}{\omega_i \cdot \mathbf{n}(1 - k) + k}, \quad (23)$$

$$D(\mathbf{h}) = G(\mathbf{h}; \mathbf{n}, \frac{2}{R^4}, \frac{1}{\pi R^4}) = \frac{1}{\pi R^4} e^{\frac{2}{R^4}(\mathbf{h} \cdot \mathbf{n} - 1)}, \quad (24)$$

where S is the specular reflectance (Fresnel coefficient), R is the roughness, and $k = \frac{(R+1)^2}{8}$.

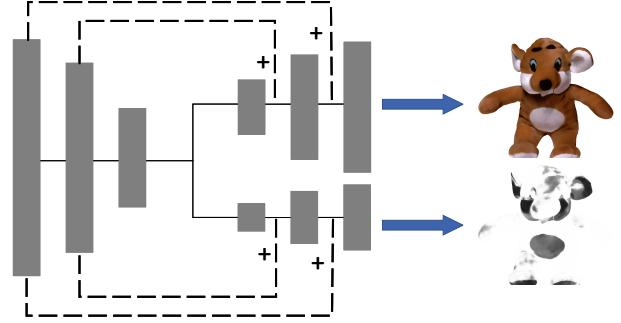
C. Non-differentiability at Tangent Lights

We present the partial gradient computation deduction for the tangent lights in one dimension for a simple explanation. The environment lights are all within a 2D plane and uniformly distributed between x_0 and x_1 , and x_θ is the tangent light that $L_i(x_i)$ change abruptly (*i.e.*, from “obstructed” to “visible”, see the supplementary video for animation) and the location is related to scene parameters θ . The rendering equation can be simplified to:

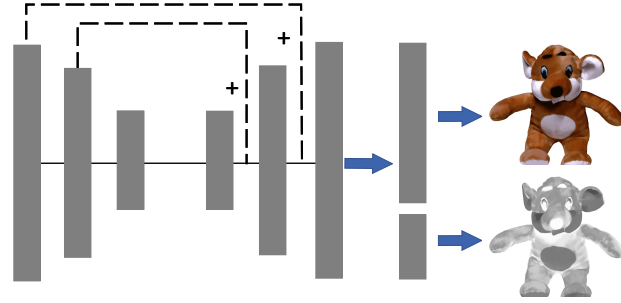
$$L_o(\omega_o; \mathbf{p}) = \int_{x_0}^{x_1} L_i(x_i) f_r(\omega_o, \mathbf{x}_i; \mathbf{p})(\mathbf{x}_i \cdot \mathbf{n}) dx_i, \quad (25)$$

where \mathbf{p} represents location of green point Fig. 9 and its surface normal \mathbf{n} . We replace $L_i(x_i) f_r(\omega_o, \mathbf{x}_i; \mathbf{p})(\mathbf{x}_i \cdot \mathbf{n})$ using $F(x_i)$ for the clean deduction.

When calculating the partial derivative of $L_o(\omega_o; \mathbf{p})$



(a) Two Separate Decoders



(b) Shared Decoder

Figure 10. **Different Material Decoders.** We visualize the structure of two different decoders. For real-world datasets, sharing more layers (b) for decoding can add regularization on roughness prediction to avoid trivial solutions occurring in (a).

w.r.t. to network parameters θ , we can get:

$$\begin{aligned} \frac{\partial L_o(\omega_o; \mathbf{p})}{\partial \theta} &= \frac{\partial}{\partial \theta} \int_{x_0}^{x_1} F(x_i) dx_i \\ &= \frac{\partial}{\partial \theta} \int_{x_0}^{x_\theta - \epsilon} F(x_i) dx + \frac{\partial}{\partial \theta} \int_{x_\theta + \epsilon}^{x_1} F(x_i) dx \\ &= F(x_\theta - \epsilon) \cdot \frac{\partial x_\theta}{\partial \theta} + \int_{x_0}^{x_\theta - \epsilon} \frac{\partial}{\partial \theta} F(x_i) dx \\ &\quad - F(x_\theta + \epsilon) \cdot \frac{\partial x_\theta}{\partial \theta} + \int_{x_\theta + \epsilon}^{x_1} \frac{\partial}{\partial \theta} F(x_i) dx \\ &= \Delta F(x_\theta) \cdot \frac{\partial x_\theta}{\partial \theta} + \int_{x_0 x_1 - x_\theta} \frac{\partial}{\partial \theta} F(x_i) dx \end{aligned} \quad (26)$$

where $x_0 x_1 - x_\theta$ means removing x_θ at the edge.

We can extend this to two-dimensional rendering integral, using Reynolds transport theorem [29]. A comprehensive high dimensional proof can be found in [8].

D. Detailed Network Architecture

Fig. 11 visualizes the detailed DIP architecture. For each network, the yellow blocks are the inputs, and the orange blocks are the outputs.

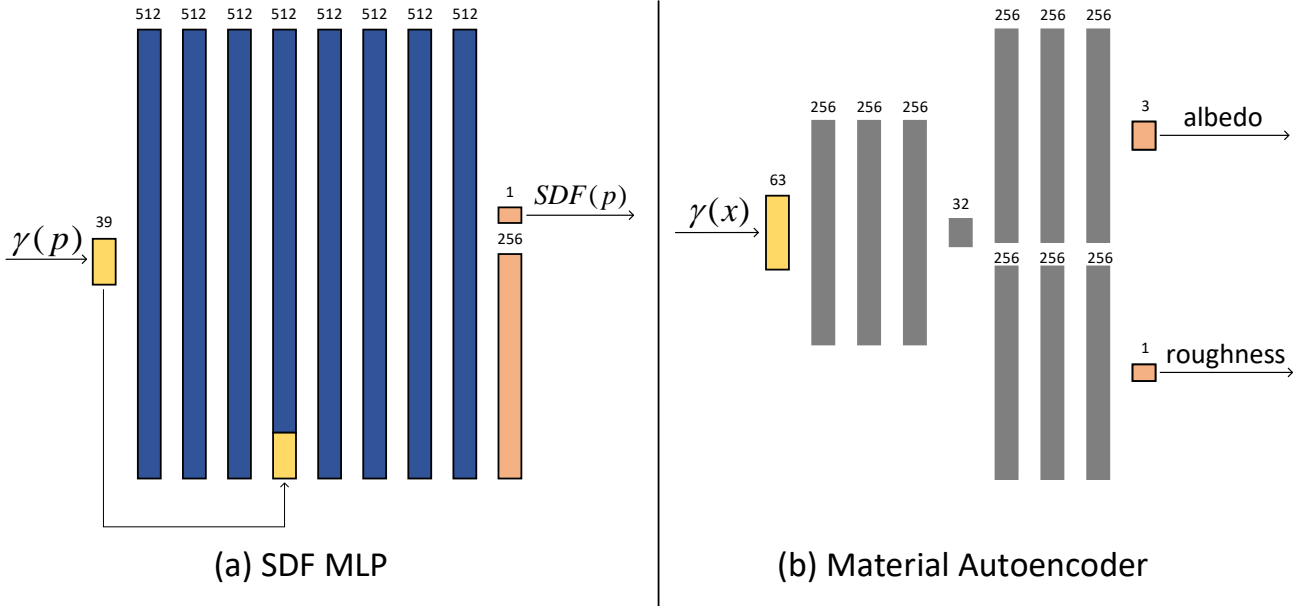


Figure 11. **Detailed DIP architecture.** (a) The SDF MLP in Sec. 4.1 in the main paper. (b) The material autoencoder in Sec. 4.4 in the main paper. (c) The indirect MLP in Sec. 4.3.1 in the main paper. $\gamma(\cdot)$ indicates the positional encoding procedure.

Fig. 11(a) shows the SDF MLP (F_{SDF} in Sec. 4.1 in the main paper). It takes the positional embedding of a query 3D point p , and outputs its SDF value and a 256 dimension feature embedding (used for geometry pre-training as [46]). The SDF MLP uses the softplus activation after each hidden layer. Fig. 11(b) illustrates the material autoencoder (Sec. 4.4 in the main paper). It takes the positional embedding of a surface point x as input and predicts the albedo and roughness at this point. Both the material autoencoder and indirect MLP (Fig. 4) use ReLU as an activation function after each hidden layer.

E. Comparisons of Material Decoders on DTU

When using the original material decoder in Fig. 10(a) for albedo and roughness estimation, we get inconsistent roughness (e.g., the bear and owl) or even trivial roughness solution (e.g., the fruits) in Fig. 12.

This inconsistency and trivial solution can be solved by replacing two separate decoders with a shared one shown in Fig. 10(b). By doing so, we implicitly add a mutual constraint on roughness and albedo prediction. Intuitively, this design is used as a regularization to smooth the estimation and avoid the trivial solution. The qualitative comparison of the two decoder designs is shown in Fig. 12.

F. More Qualitative Results

Qualitative Results of Inverse Rendering. Though MII [46] can disentangle roughness and albedo, the estimated roughness lacks consistency and is prone to strong re-

flectance lights (e.g., the edges of the balloons and ketchup on the hotdogs). MII [46] also struggles to distinguish the different roughness of the three jugs. Comparisons of our method with PhysSG [43] and MII [46] are shown in Figs. 13 to 16.

Qualitative Results of Tangent Lights’ Contribution. We visualize the qualitative results of including tangent lights or not. Though the inverse rendering results (i.e., albedo and roughness estimation) are similar, our full model achieves better light estimation results, as demonstrated in Fig. 17.

G. Limitations

Because self-supervised inverse rendering is a highly ill-posed problem, our method sometimes has difficulty disentangling geometry and texture. As shown in Fig. 13, the strips on the board under the jars are predicted as grooves but actually are the texture patterns of the board. Either ground truth supervision or prior knowledge is required to resolve this issue.

Another limitation of our method derives from the assumption we make for indirect light estimation – we assume that the objects’ Fresnel coefficient [3] is fixed to be 0.02, meaning the diffuse dominates at x' in Fig. 11. As a result, specular is omitted at x' (it is still considered when rendering point x), and our method can not accurately predict the inverse rendering of a mirror-like object (though we can change from the porcelain material to a mirror surface). A potential solution is to pre-train on an annotated dataset as a prior. We leave these limitations to future work.



Figure 12. **Qualitative Comparison of Two Decoders on DTU [13]**. Using separate decoders makes the model predict saturated roughness. This phenomenon can be resolved by sharing more layers between the roughness and albedo decoder.

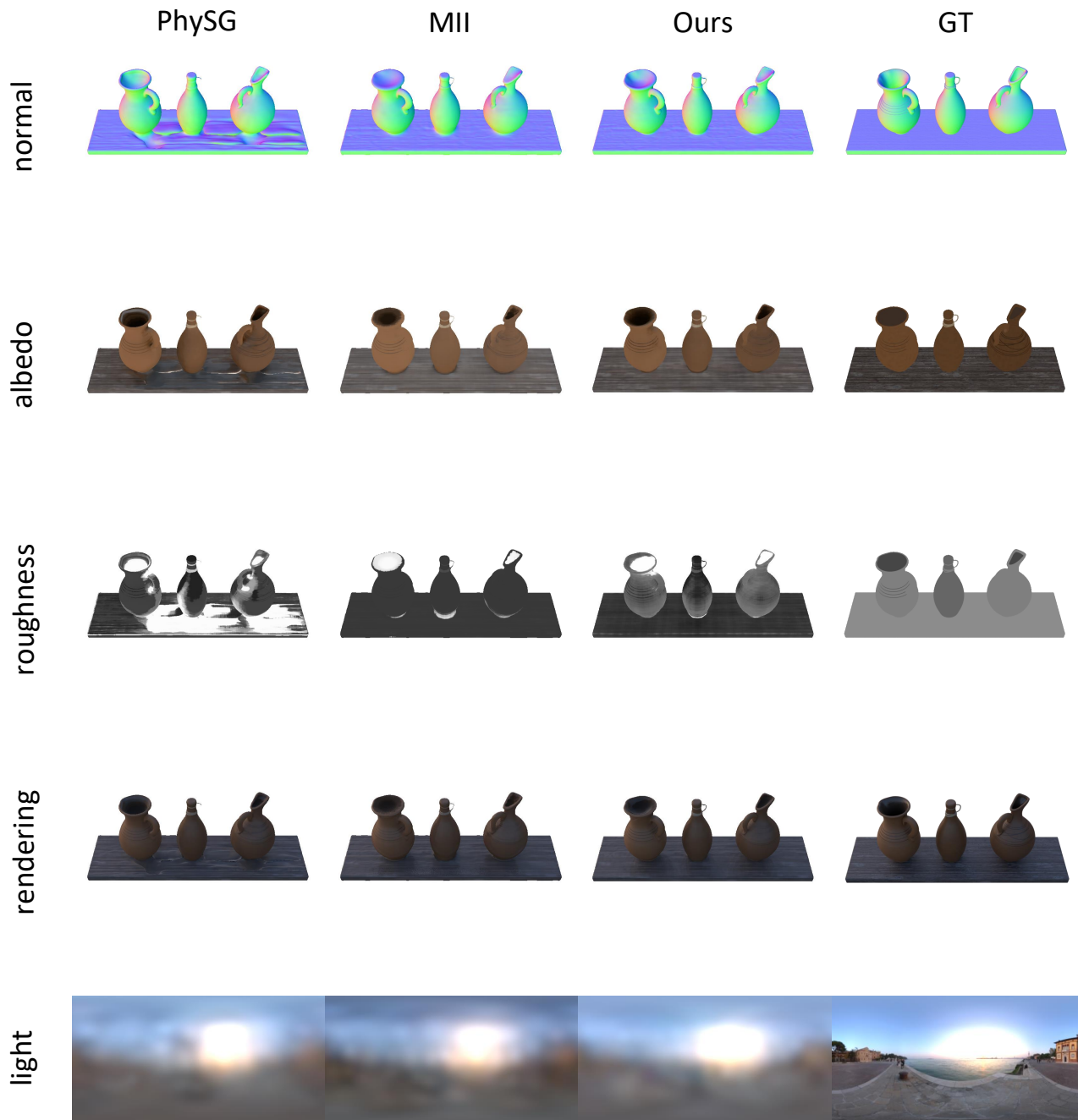


Figure 13. **Qualitative Results on Jugs.** PhySG [43] can not disentangle shadow and albedo where the area is occluded, while MII [46] has difficulty distinguishing the jugs’ roughness differences. Moreover, our model produces a more reasonable light estimation compared with the two baselines.

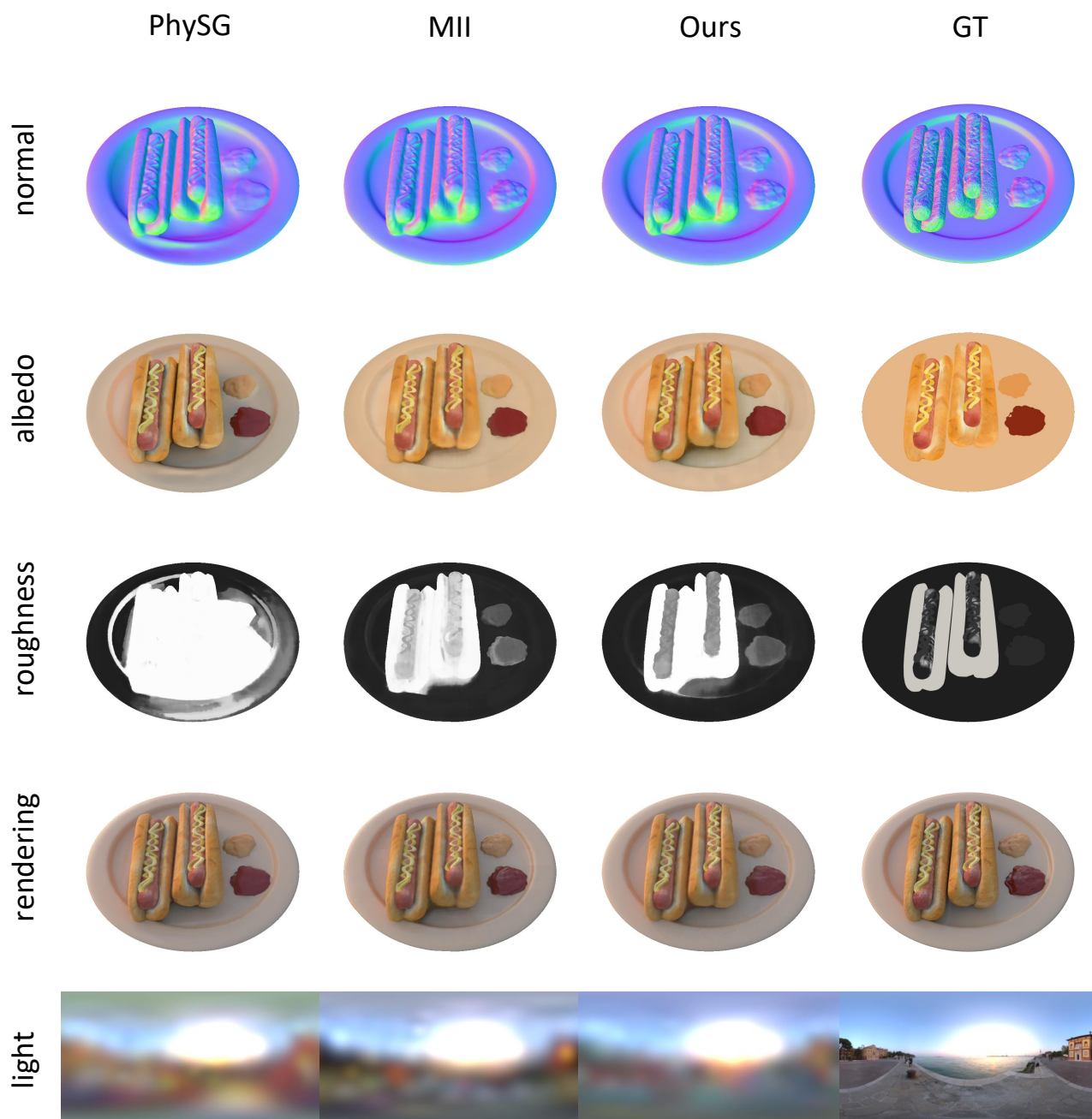


Figure 14. **Qualitative Results on Hotdog.** PhySG [43] completely fails to predict the roughness of the hotdog, and the roughness of MII [46] is noisy. Moreover, the light estimation of these two baselines is not as consistent as the proposed method.

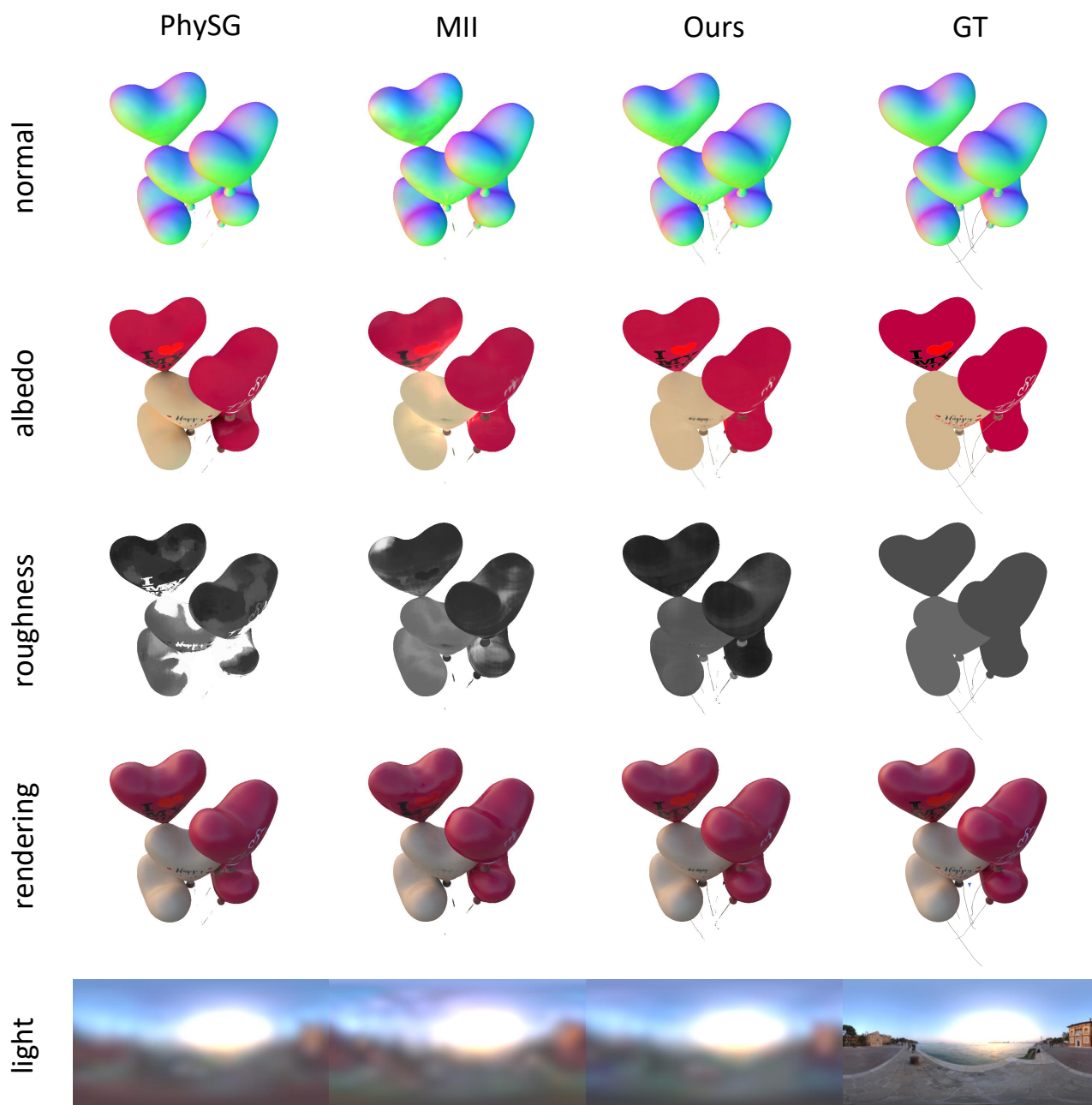


Figure 15. **Qualitative Results on Balloons.** PhySG [43] fails to disentangle the shadow of the balloons and cannot predict the roughness under occlusion. MII [46] presents artifacts at the edges of the balloons.



Figure 16. **Qualitative Results on Chair.** PhySG [43] and MII [46] predict inaccurate albedos with lighter colors than the ground truth albedo.

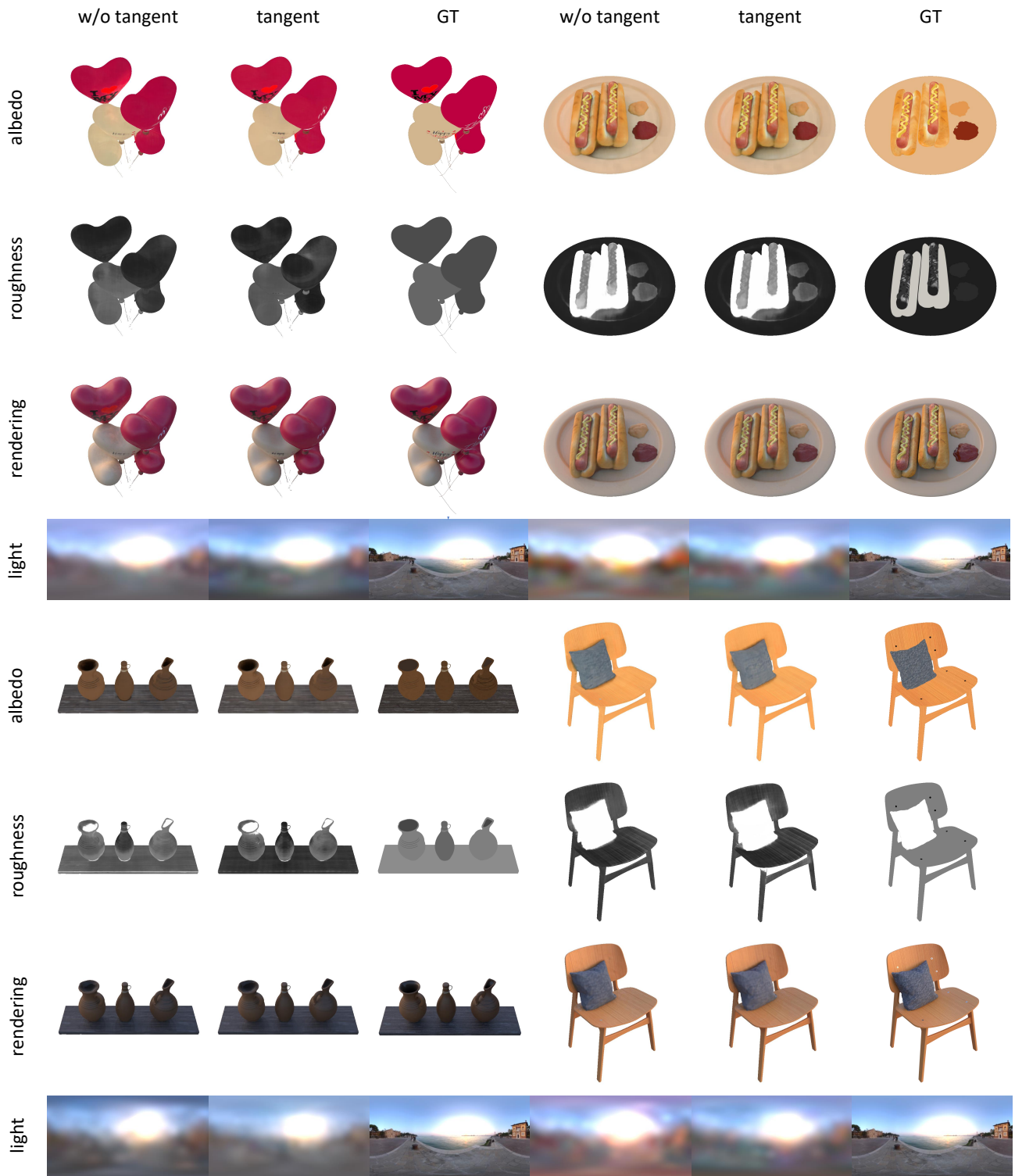


Figure 17. **Ablation studies on tangent lights.** Our full model can achieve better light estimation results by considering tangent lights.